Earth Surf. Dynam. Discuss., doi:10.5194/esurf-2017-20, 2017
Manuscript under review for journal Earth Surf. Dynam.
Discussion started: 12 April 2017

Spatiotemporal patterns and triggers of seismically detected rockfalls

Michael Dietze[1], Jens M. Turowski[1], Kristen L. Cook[1], and Niels Hovius[1]
[1]GFZ German Research Centre for Geosciences, Section 5.1 Geomorphology, Potsdam, Germany
Correspondence to: Michael Dietze (mdietze@gfz-potsdam.de)

Abstract.
Rockfalls are an essential geomorphic process and an important natural hazard in steep landscapes across the globe. Seismic monitoring can provide precise information on the timing, location and event anatomy of rockfalls, parameters that are otherwise hard to constrain. By pairing data from 49 seismically detected rockfalls in the Lauterbrunnen Valley, Swiss Alps, with independent information about potential triggers during autumn 2014 and spring 2015, we are able to i) analyse the evolution of single rockfalls and their common properties, ii) identify seasonally changing activity hotspots, iii) and explore temporal activity patterns at different scales, ranging from months to minutes, to quantify relevant trigger mechanisms. Seismic data allows the classification of rockfall activity into three distinct phenomenological types and can be used to discern multiple rock mass releases from the same spot, identify rockfalls that trigger further rockfalls and resolve modes of subsequent talus slope activity. In contrast to findings based on methods with longer integration times, rockfall in the monitored limestone cliff is not spatially uniform but shows a downward shift of rock mass release spots by 33 m per month over the year, most likely driven by a continuously lowering water table. Freeze-thaw-transitions account for only 5 out of the 49 rockfalls whereas 19 rockfalls were triggered by rainfall events, with a peak lag time of 1 h. Another 17 rockfalls were triggered by diurnal temperature changes and occurred during the coldest hours of the day as well as during the highest temperature change rates. This study is thus the first one to show direct links between proposed rockfall triggers and the spatio-temporal distribution of rockfalls under natural conditions, and extends existing models by providing seismic observations of the rockfall process prior to the first rock mass impacts.

1 Introduction

Rockfall is a fundamental geomorphic process in alpine landscape dynamics and an important natural hazard. Knowing where, when and due to which triggering mechanism rockfalls occur and how they evolve are essential questions. However, rockfalls involve the infrequent and rapid mobilisation of comparably small volumes of rock, which are difficult to observe directly. As a consequence, precise constraints on timing, location and triggers are hard to come by. There are many established approaches to detect rockfall activity spatially, for example surveys of talus slopes, dendrometric and lichenometric approaches (Krautblatter et al., 2012; Stoffel et al., 2005; Matsuoka and Sakai, 1999), and more recently image-based mapping as well as terrestrial and airborne laser scanning (Stock et al., 2011; Strunden et al., 2014; D'Amato et al., 2016). The temporal information delivered

Earth Surf. Dynam. Discuss., doi:10.5194/esurf-2017-20, 2017
Manuscript under review for journal Earth Surf. Dynam.
Discussion started: 12 April 2017

by these methods is not very precise, typically on the order of weeks to years. D'Amato et al. (2016) were able to narrow the temporal resolution to the sub-daily level during a study of a limestone cliff. They analysed 10 minute interval photo imagery together with terrestrial laser scan data for a period of 887 days, which resulted in a data base of 144 rockfalls with a time uncertainty of less than 20 h for some of the events. However, in general, it has so far been difficult to link detected rockfall events to potential trigger mechanisms by temporal coincidence, and to investigate potential early warning signals at or below hourly resolution.

Seismic sensors provide a valuable complement to the above mentioned methods. They allow precise temporal fixes of rockfall event initiation and duration. If the sensors are deployed as a seismic network, they further allow source location estimates with uncertainties of tens of metres (Burtin et al., 2014; Hibert et al., 2014; Dietze et al., 2017), enabling direct temporal and spatial links to potential triggers. Furthermore, seismic signals allow insight into the anatomy of geomorphic processes by interpretation of the recorded time series and spectral properties. During the last decade, there has been significant scientific progress in theory (Gimbert et al., 2014; Larose et al., 2015), experiments (Farin et al., 2015; Vilajosana et al., 2008), and application across different scales (Dammeier et al., 2011; Lacroix and Helmstetter, 2011; Zimmer et al., 2012; Ekström and Stark, 2013; Burtin et al., 2016). However, rockfall activity has mainly received attention as "by-product" of seismic observatories with different scopes (e.g., Helmstetter and Garambois, 2010; Hibert et al., 2011; Burtin et al., 2014) and research has focused on linking seismic properties with geometric and kinetic characteristics, such as mobilised volume, run out length or fragmentation (Dammeier et al., 2011; Ekström and Stark, 2013; Hibert et al., 2014). Systematic linking of events to more than one potential environmental trigger has received only marginal attention (Helmstetter and Garambois, 2010; Burtin et al., 2013).

We employ environmental seismology, the study of the seismic signals emitted by Earth surface processes, in the Lauterbrunnen Valley, a steep rockfall-prone cliff in the Bernese Oberland, to detect and locate rockfalls during a more than six month long monitoring period. We interpret the seismic data to gain insight into the individual stages and overall phenomenological types of rockfall events. Based on rockfall event lag times, we discuss the significance of different trigger mechanisms. Combining spatial and temporal patterns of rockfall activity, we reveal a consistent seasonal shift of a rockfall activity window down the cliff and quantify the effect of diurnal forcing on rockfall activity.

2 Anticipation of rockfall triggers

Rockfall is the result of the formation of an isolated volume of rock from the source rock mass (block production phase) and its subsequent detachment by a release mechanism activated by a driving force (trigger phase). Block production can be attributed to several processes, such as crack propagation and solution of solids (Krautblatter et al., 2012), and usually acts over several months to years. The release mechanism is essentially a decrease in the stabilising forces (e.g., frictional force, cohesion force) until their sum is smaller than the gravitational force acting on the rock mass. This decrease can occur suddenly or gradually, depending on the trigger. Thus, we broadly follow Wieczorek (1996) in defining a trigger as an external stimulus that causes a near-immediate geomorphic response by decreasing material strength or increasing stress. Implicit to this definition is that some triggers have nearly immediate response while others require a certain response time or minimum cumulative impact duration. Rockfall triggers are numerous and hard to assign to a specific event (Stock et al., 2013). The relationship between cause (trigger) and effect (rockfall) is predominantly constrained based on temporal coincidence with almost no or only very generalised information on spatial coincidence. Many trigger mechanisms can overlap, be superimposed, or have additive effects, which makes it difficult to pinpoint individual processes based on only response time lags. In the following paragraphs we review relevant rockfall triggers in terrestrial environments. They cover the dominant mechanisms that are supposed to lead to rockfall and the expected range of time lags between trigger activity and rockfall response for each mechanism. This list builds the foundation for relating the identified rockfall events from this study to external stimuli, i.e., to conduct a posterior process-response analysis.

2.1 Geophysical triggers

Earthquakes, as well as volcanic tremors and eruptive activities, generate seismic waves that result in ground acceleration and thus mechanical stress through inertial forces (Hibert et al., 2014). When this force overcomes a given threshold (e.g., set by friction or cohesion force), the rock mass can be mobilised. A typical proxy for geophysical trigger intensity is peak ground acceleration. If this acceleration overwhelms gravitational acceleration, a free resting object can be moved. The reaction of a rock mass to excitation by an earthquake is almost immediate, i.e., during or within seconds after the trigger.

2.2 Mass wasting processes

Snow avalanches can dislodge and entrain loose rocks by direct impacts or basal shear stress (Stock et al., 2013). However, snow avalanches rarely occur on cliff faces because these are too steep to support massive continuous accumulations of snow. In such terrain, ice falls are more likely to occur wherever frozen waterfalls exist. Slope failures can also be a caused by destabilisation and ground motion induced by other mass movements or fluvial activity as has been shown for debris flows and rock avalanches in the Illgraben, a steep catchment in the Rhone Valley (Burtin et al., 2014). The response of a rockfall to other mass wasting processes is supposed to be immediate.

2.3 Meteorological triggers

Precipitation, particularly in the form of rain and subsequent run off, can affect rockfall activity through several mechanisms. It can increase the weight/load of a rock volume, reduce pore pressure and thus cohesion, lead to expansion of clay minerals, erode cohesive fine material from cracks and dissolve rock compounds (Stock et al., 2013). The reaction time of a rockmass to precipitation depends on the exact mechanism. Increasing the load requires time for rain water infiltration, percolation and retention inside the rockmass. Thus, rainfall amount and surface permeability are further important control factors. Pore pressure decrease also occurs after percolation until, eventually, the entire regolith or rock mass is saturated. Both processes may show lag times of several hours, depending on the local hydrology. Even longer lag times are to be expected for swell-shrink effects of clay minerals.

Wind interaction with bare rock surfaces results in pressure fluctuations and thus cyclic stress. Trees or other perennial species can cause a local leverage effect, especially when their roots have penetrated into cracks and fissures of a rock mass (see also section 2.5). The response of a rockmass to excitation by wind should be immediate as there is no mechanism that would cause a time lag.

Lightning can contribute to rock fracturing and mobilisation by the massive electric discharge that is able to vaporise water and thus increase gas pressure within the rock. There has been speculation about the role of lightning in the erosion of mountain summits (Knight and Grab, 2014). There should be no time lag between lightning strike and rockfall activation.

2.4 Heat-related triggers

This group includes two mechanisms: freeze-thaw dynamics and thermal stress. Freeze-thaw actions as rockfall triggers can work in two directions: transitions from the solid to the liquid state and vice versa (D'Amato et al., 2016, and references therein). During thawing, the stress field created by the interplay between rock structure and ice-filled cracks and fissures changes suddenly. Additional melt water is produced, with consequences for the rock mass similar to those of water from precipitation. During freezing, volume expansion through ice formation drastically increases rock-internal pressure but also increases the cohesion along rock joints, which has a positive effect on bulk rock strength. A further process is the warming of ice below the melting point, which can cause pressure to increase due to thermal dilation. The lag time between a recorded freeze-thaw or thaw-freeze transition and a rockfall can be transgressive, as the trigger process itself is transgressive, too. D'Amato et al. (2016) find the most common response times at their highest resolution level (< 20 h), which means that slope reaction to free-thaw transitions can be expected to be 20 hours or less.

Thermal stress results from rock deformation due to heat-driven dilation or contraction. This cyclic mechanism can prepare blocks by driving crack propagation and finally cause the failure itself (Collins and Stock, 2016). Furthermore, material that falls or is washed into the opened fissures prevents the fissure from closing again and thus further increases stress. There are two parameters of interest: the extreme states of deformation (maximum contraction and maximum expansion) and the deformation rate. The time lag between thermal forcing and rockfall results primarily from heat diffusion into the rock mass and the subsequent deformation. Calculations and in situ measurements by Collins and Stock (2016) for heating a 10 cm thick granitic rock slab in a rockfall prone environment by 20 K suggest a diffusion time of about 3 hours. Thus, for propagating a heat pulse through the first few decimetres of rock, time lags of several hours can be expected.

2.5 Biotic/anthropogenic triggers

Biological triggering of rockfalls can be through animal traffic on loose rocks as well as vegetation growth. The latter results in a growing load with time, leaching of mineral components, and also the expansion of rock fractures by the root system and leverage effects through interaction with wind. We are not aware of a study that explicitly links the effects of biological activity to rockfall activity. Thus, a time lag discussion for this trigger would be highly speculative.

Human activity is manifold. It can cause rockfall by ground vibrations due to transport activity such as train or road traffic, construction work (including resulting terrain disturbance), and blasting, as well as direct rock dislodgement by people passing on foot or climbing. The response of rockfall to this trigger mechanism is supposed to be immediate.

3 Materials and methods

3.1 Study area

The Lauterbrunnen Valley (figure 1) is a spectacular Alpine valley with about 1000 m high, nearly vertical (88.5 °) Mesozoic limestone cliffs, which are dissected by several hanging valleys. 150 m high talus slopes at the base of the cliff, in many locations covered with fresh debris, suggest substantial and sustained rockfall. In winter, the rock wall is snow-free, but the waterfalls usually freeze. The steepest section of this rockfall-prone valley, located between the towns of Mürren and Lauterbrunnen, has been investigated in an earlier study, where terrestrial laser scan data was combined with seismic data (Dietze et al., 2017). This combination of methods allowed pairwise detection of ten rockfall events within one month, ranging from 0.053 ± 0.004 to 2.338 ± 0.085 m^3, with location differences of 81^{+59}_{-29} m. Thus, for this area (about 2.16 km^2) the data processing work flow and validation of the seismic approach has already been developed. Under the current conditions, rockfall activity mobilises small volumes, usually below 1 m^3, and appears to be more or less equally distributed throughout the monitored cliff faces when integrated over several months (Strunden et al., 2014). In contrast, when determining event timing and location at sub-diurnal intervals (Dietze et al., 2017), events are highly episodic and spatially non-uniformly distributed.

3.2 Equipment and deployment

Seismic activity was monitored by six broadband seismometers (Nanometrics Trillium Compact 120s). The instruments were deployed during two observation periods: July 30 to October 28 2014 and March 17 to June 24 2015. Ground velocity signals were recorded with Omnirecs Cube ext^3 data loggers, sampling at 200 Hz (gain of 1, GPS flush time 30 minutes). Deployment sites were chosen to optimise the potential for location along the east-facing rock wall below the town of Mürren. Stations were separated from each other laterally by 1100 to 1300 m and vertically by 700 to 1000 m. Three stations were deployed along the upper limits of the talus cones at the foot slope and three stations were set up on top of the cliff (cf. figure 1). Each seismic sensor was installed in a small hand dug pit at 30 to 40 cm depth, seated on bedrock where possible.

For locating the seismic sources due to rockfall, a digital elevation model (DEM) of the wider study area with 5 m grid size (swissALTI3D) was projected to the UTM system and resampled to 10 m grid size. For quality assessment and source location projection along the vertical cliff, a high resolution topographic model of the valley wall was created using terrestrial lidar data collected with a Riegl VZ-6000 scanner in March 2014. Scans collected from four different vantage points were combined and the resulting point cloud was subsampled to obtain a resolution of 1 m. Hourly data of air temperature, precipitation and global radiation from a weather station in Mürren (cf. figure 1, data from Meteomedia) were analysed to relate the identified rockfall events to meteorological triggers.

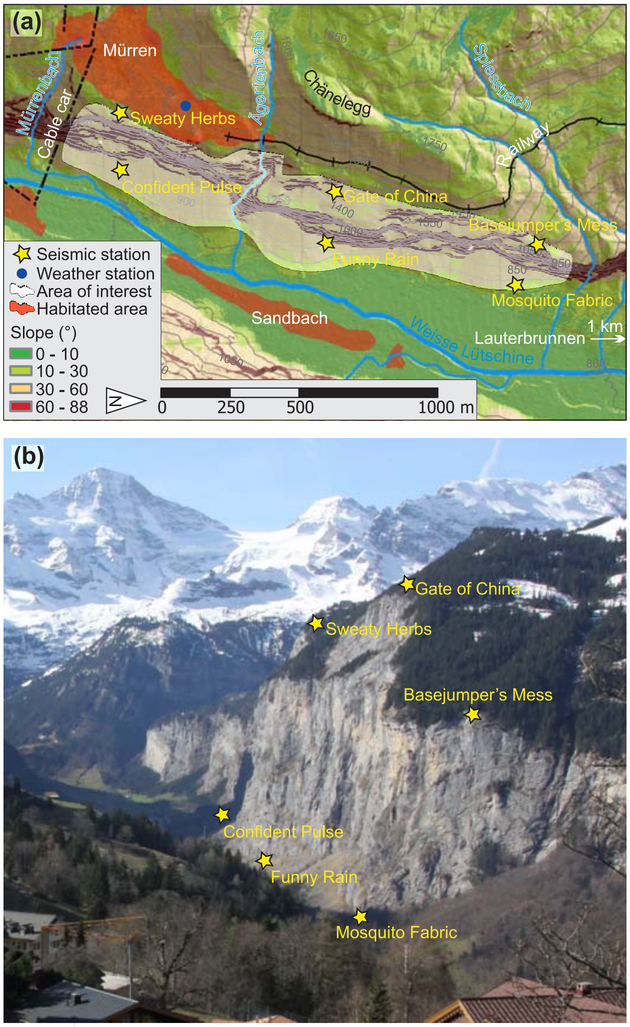

Figure 1. The study area Lauterbrunnen Valley. a: Schematic map with location of seismic stations and weather station as well as anthropogenic noise sources (settlements, technical infrastructure). b: Photograph of the instrumented east-facing rock wall.

3.3 Seismic data analysis

Detection of rockfall events was performed as described by Dietze et al. (2017) and summarised as follows. The vertical component signal of the central station "Gate of China" was screened for seismic events using a short-term-average/long-term-average (STA/LTA) ratio picker (Havskov and Alguacil, 2006). This algorithm is sensitive to instantaneous rises in the ground velocity and can be used to define the start of an event (on-threshold ratio) and the end of an event (off-threshold ratio), i.e., to extract discrete events from the continuous stream of seismic data. For this, the hourly raw signal files from both monitoring campaigns were appended to 25 hour long traces, overlapping by one hour. These time series were filtered between 10 and 30 Hz, the typical frequency band of rockfalls and rock avalanches (Helmstetter and Garambois, 2010; Hibert et al., 2014; Burtin et al., 2016; Dietze et al., 2017), and their signal envelopes (i.e., the square root of the squared Hilbert transform of the signal) were calculated. The STA/LTA picker was run with a short term window of 0.5 s and a long term window of 90 s. The on-threshold was set to 5, the off-threshold was set to 2. The long-term average value was set constant after the start of an event (cf. Burtin et al., 2014). Following Dietze et al. (2017), events that were longer than 20 s (typically earthquakes) or were shorter than 0.5 s (typically local raindrop impacts) were removed. Likewise, events with a signal-to-noise-ratio (SNR, defined as ratio of maximum to mean signal amplitude of a picked event) below 6 were removed. Further events were excluded when the time delay with which their signal arrived at the seismic stations was higher than the time a seismic wave would need to travel through the array, which was 1.4 s (cf. Dietze et al., 2017). To do so, STA/LTA results of all other stations for the picked event with a two-sided buffer of 1.4 s were checked for coincidence. Only when an event was detected by at least three seismic stations the result was kept. When two or more events were identified within less than 12 s (the maximum free fall duration from the top of the cliff), only the first one was kept and the others were treated as potentially successive impacts of the rockmass at lower cliff sections.

Ten rockfall events in the Lauterbrunnen Valley that were detected by laser scanning as well as seismic methods (Dietze et al., 2017) had seismic characteristics that are different from those of previously published rockfalls or rock avalanches in less steep terrain, which usually show emergent waveforms with slow rising and falling seismic signal time series (Helmstetter and Garambois, 2010; Hibert et al., 2014). In the Lauterbrunnen Valley, the released rockmass typically experiences a significant free fall phase, followed by a powerful impact either somewhere on the cliff or directly on the talus slope. The impact may result in fragmentation of the initial rockmass and/or mobilisation of detritus on the talus slope. Thus, rockfalls in the study area have a distinct seismic signature in comparison to earthquakes and other mass wasting processes, as for example compiled by Burtin et al. (2016). All remaining potential rockfall events were manually checked for agreement with these patterns (cf. Dietze et al., 2017).

In addition to the waveforms of potential events, their spectral evolution with time was investigated using power spectral density estimates (PSD, or spectrograms). These were calculated for the event duration plus a two-sided buffer of 30 s, using multi taper correction of the spectra and the method of Welch (1967). The spectra were calculated from the deconvolved and filtered vertical component of the signal (1–90 Hz) at the central station along the cliff base (“Funny Rain”) with time windows of 1.1 and 1.5 s and overlaps of 90 %. Rockfall impacts appear as sharp pulses of seismic energy over a wide frequency band, usually between 5 and 60 Hz (Lacroix and Helmstetter, 2011; Hibert et al., 2014; Dietze et al., 2017). Rock avalanches show a triangular evolution with an emergent onset dominated by low frequencies, progressively increasing higher frequency content until the event ends with the prevalence of low frequencies (Suriñach et al., 2005). Earthquakes show the dominance of frequencies below 5 Hz and either two distinct wave train arrival times followed by an exponentially decreasing tail (coda) or a very low frequent waveform (teleseismic events). Anthropogenic signals can take a range of forms in this area (cf. Dietze et al., 2017).

For all manually confirmed rockfall signals the source location was estimated by the signal migration method (Burtin et al., 2014). This approach is based on finding the location with the highest joined cross correlation of signal envelopes from all station pairs with time offsets. These time offsets correspond to the finite travel time of the signal from a potential source along the surface or through bedrock to each seismic station. For this, the average seismic wave velocity was set to 2700 m/s (cf. Dietze et al., 2017). The input signals were clipped to their STA/LTA-based start and duration plus a two-sided buffer of 2 s unless manual modification was necessary, e.g., when obviously unrelated seismic signals like rain drop impacts at one station had biased the process or when two consecutive impacts had been included. The clipped signals were filtered with four different initial cut off frequencies and the location result with the highest joined cross correlation value was kept. These initial frequency windows were 5–15 Hz, 10–20 Hz, 10–30 Hz and 20–40 Hz. When an event could not be located in the area of interest (fig. 1) but showed all characteristics of a valid rockfall event, the frequency windows were adjusted according to the dominant frequency range. The migration operations resulted in grids with joined cross correlation values for each pixel, which may be interpreted as a probability estimate of the most likely location of the impact that causes the seismic signal. In accordance with the findings of Dietze et al. (2017) only pixels with cross correlation values above the quantile 0.97 were kept, as this threshold resulted in the smallest possible location estimate area that still included all ten control events. The resulting data sets were normalised between 0 and 1 to have a common base for further analyses.

3.4 External trigger analysis

All identified rockfall events were put into context with potential trigger mechanisms by calculating the lag time to the closest preceding occurrence of each potential trigger. Depending on the mechanism, automatic algorithms or manual checks were necessary, as explained below.

Lag time distribution patterns for all detected rockfalls were inspected by kernel density estimates (KDE, i.e., curves that describe the distribution of discrete empiric data). It is known that the size of the kernel (i.e., the window that is moved over the sample distribution to create the density estimate) has significant impact on the resulting curves, especially for small sample sizes (Galbraith and Roberts, 2012; Dietze et al., 2016) and there is no general rule to find the best setting. To account for this effect as well as to check the general robustness of the temporal patterns, multiple KDE graphs were generated based on Markov Chain Monte Carlo methods. For each test, the complete data set of rockfall events was subsampled 1001 times with a random sample size between 80 and 100 % and randomly assigned kernel bandwidths. This resulted in 1001 possible realisations of density estimate curves, which were all plotted over each other to create a “ghost graph” (Blaauw, 2012) that gives a direct impression of the uncertainty associated with this method.

3.4.1 Excluded triggers

The setting of the Lauterbrunnen Valley already allows for the elimination of some of the trigger mechanisms summarised in section 2. Volcanic tremors and eruptive activities are very unlikely to influence this region of the Alps, as the nearest active volcano is Vesuvio. Snow melt-generated water input is regarded as irrelevant because the cliff face is snow free in winter due to the steep gradient. Only the small ledges may support accumulations of snow that could supply local input of melt water.

Snow melt may be a significant source of water input in the upper parts of the catchment, above the cliff face, but this run off would already be channelised in the hanging valleys by the time it reaches the cliff. It can thus be neglected as a mechanism significantly affecting material properties outside the hanging valleys. Likewise, snow avalanches are unlikely to influence rockfall activity along the cliff face. Root penetration of trees is considered to be of minimum relevance given the steepness of the cliff; trees only grow on the flat parts of the large ledges in the central upper section and at the southern margin of the instrumented cliff section. Thus, these trigger mechanisms are not considered further in the article, reducing the analysis to the following mechanisms.

3.4.2 Geophysical triggers

Earthquakes were picked from the signals recorded by the seismic sensors with the STA/LTA approach using a 1 s short term window, a 90 s long term window as well as on- and off-ratios of 4 and 2, respectively. The protocol was applied to data from station “Gate of China”, filtered between 1 and 5 Hz, with a minimum event duration of 3 s. All picked events were checked manually for plausibility. Furthermore, the online portal of the Swiss Seismological Survey (Service) was queried for any earthquake above Mw 1 that occurred within a radius of 20 km around the study area.

3.4.3 Meteorological triggers

Lag times for precipitation were defined as the time span between a precipitation event with > 0.1 mm h^{-1} (the smallest increment of the meteorological data set) and the next rockfall. For each of these precipitation events the cumulative amount was calculated by summation backwards in time until the onset of the precipitation event.

Wind as trigger was investigated using the meteorological time series data. Wind speed values were selected for the hour during which a rockfall occurred. Effectiveness of wind was tested by comparing the event-coinciding wind speed distribution function with 1001 randomly generated distribution functions for the entire monitoring period. If the wind speed regime during a rockfall is different from random regimes, this would be visible from this comparison. Since wind is assumed to be a regional phenomenon, a point measurement of wind speed at the station in Mürren is assumed to be representative.

For the effect of lightning there is no independent record. However, thunder also generates a seismic signal. The frequency spectrum of such a thunder signal is similar to quarry blasts, and is very broad (above 5 Hz) with peak frequencies between 6 and 13 Hz. Seismic records can be inverted to determine the location, length and orientation of a lightning channel (Kappus and Vernon, 1991). In the case of the Lauterbrunnen valley, one hour of the seismic record preceding a detected rockfall event was screened for all stations. Lightning was interpreted when the signals showed a sharp blast-like pulse, time offsets between stations corresponding to the speed of sound (about 340 m/s), a wide frequency spectrum peaking between 5 and 15 Hz, and a coincidence with precipitation (assuming there were no dry weather lightning events).

3.4.4 Heat-related triggers

Freeze-thaw and thaw-freeze transitions were defined as switches from negative to positive (and vice versa) air temperatures during two consecutive hours. Constraining the thermal effect within rock is not a straightforward task. Direct measurements require intense instrumentation (Collins and Stock, 2016). Geophysical tomography monitoring (Krautblatter et al., 2010) from the rock surface is an alternative but also requires extensive work. Heat diffusion models (e.g., Martinez et al., 2014) can deliver temperature estimates at different levels of spatial and temporal resolution and complexity; however, at first order, air or surface temperature is a valuable proxy for describing the freeze-thaw actions close to the surface of rock masses. In contrast to wind, temperature cannot be treated as a regionally constant parameter. Air temperature drops by 0.6 ° C for every 100 m rise in elevation, and mountain wind systems and topographic shading effects contribute to further modifications of spatial temperature patterns. To relate air temperature as a first order proxy to freeze-thaw action, lag times were calculated for both uncorrected temperature data from the Mürren meteorological station and elevation-corrected values based on the DEM and the seismically located rockfalls events.

Constraining thermal stress is similarly demanding as is freeze-thaw action. One needs to link the heat influx (through sunlight exposure and/or ambient temperature) to the thermodynamic properties of the rock medium (cf. Collins and Stock, 2016). Again, first order proxies for the susceptibility of a rockmass to thermal stress can be provided by the ambient air temperature time series and its first derivative (temperature change rates) and spatially resolved sun exposure models, although more complex models are available (e.g., Haberkorn et al., 2016). To investigate thermal stress, the temperature history of rockfall events was described with linear regression slopes of air temperature (Mürren station data) in time windows of 12, 6 and 3 hours before an event occurred. Thermal stress is also linked to the exposure duration of a given section of the cliff to direct sunlight, at the diurnal and seasonal time scale. The Lauterbrunnen Valley with its almost North-South oriented cliffs may indeed exhibit great spatial and temporal variability of exposure time to direct sunlight. The topography-corrected potential exposure time to direct sunlight of the cliff face was modelled with the regional DEM (about 30 by 30 km around the instrumented area). Calculations were performed for March 1 and 31 2016, extracting the cumulative daily exposure time for each pixel of the DEM and also extracting the lowest sunlit elevation along the cliff for a set of hours (8:00, 8:30, 9:00, 10:00, 12:00 am, 1:00, 2:00 pm) through the entire month. March was chosen because it is expected to yield the largest variability in sun exposure of all instrumented months.

3.4.5 Biotic/anthropogenic triggers

Anthropogenic activity such as construction work, train traffic, helicopter flights and road traffic in the valley was observed throughout the deployment and maintenance campaigns and can easily be detected in the seismic records (see Dietze et al. (2017) for examples and handling). Due to the broad range of possible signals generated by anthropogenic activity it is not straightforward to develop automatic routines to analyse the lag times with rockfalls. Thus, the history of each potential rockfall event was investigated manually up to one hour back in time.

Ground vibrations caused by other Earth surface processes were also checked manually by screening one hour seismic data before the onset of a rockfall event to identify any signals that could be interpreted as geomorphic activity (cf. Burtin et al., 2014; Turowski et al., 2016, for examples).

All analyses were performed in the R environment for statistical computing (R Development Core Team, 2015) (version 3.3.1) using the packages eseis (Dietze, 2016), sp (Pebesma and Bivand, 2005; Bivand et al., 2013; Pebesma and Bivand, 2016, version 1.2-3), raster (Hijmans, 2016), fields (Nychka et al., 2015), insol (Corripio, 2014) and rgl (Adler and Murdoch, 2016). Dates and times of all events are given with respect to the local time, i.e., UTC minus 2 hours. For the 2015 period, this includes 12 days without daylight saving time (switch was on March 29), which was ignored here.

4 Results

4.1 Detection and location of seismic events

During both deployment periods there were always at least four seismic stations in operation, continuously recording data. The STA/LTA picking algorithm yielded initial numbers of 3248 (2014) and 1514 (2015) events. After application of the automatic rejection criteria the number decreased to 603 and 271, respectively. Manual inspection and rejection removed predominantly spurious events (582 and 231), for example related to rail traffic and small earthquakes. The remaining potential rockfalls (21 and 40) were migrated and yielded a total of 17 rockfalls inside the area of interest for 2014 and 32 for 2015. The remaining rockfalls were located either on the other side of the valley or higher up in the catchment and will not be discussed further. The supplementary material contains a comprehensive table with all detected rockfall events along with their assigned parameters.

The average duration of the picked events was $1.14^{+0.79}_{-0.46}$ s (median and quartiles) in 2014 and $1.56^{+0.67}_{-0.54}$ s in 2015 (global average was $1.37^{+0.84}_{-0.37}$) s, which was clearly different from other signals excluded during the selection process (raindrop impacts and earthquakes). Note however, that the STA/LTA algorithm usually picked the first rockfall impact and all subsequent impacts were rejected from the data set if they occurred within 12 s (cf. chapter 3). Thus, the STA/LTA-based durations do not represent a realistic estimate of the true event duration, which has been assigned based on manual inspection of waveform and PSD data. An event from April 6 2014 (figure 2) had a picked duration of 10 s, according to its prolonged activity after the first excursion of the seismic signal. The average SNR of all events was $15.47^{+10.04}_{-2.00}$. For events 41 and 44 (cf. table S1) the per-station-SNR for location had to be adjusted to 6 and 4, respectively.

Earthquake detection for lag time analysis yielded a total of 359 events, lasting on average $14.9^{+28.3}_{-6.4}$ s. The query of the Swiss Seismological Service data base did not yield any earthquake with Mw > 1 within a radius of 20 km during the monitoring period.

4.2 Rockfall characteristics

Based on the waveform and PSD data of all events, rockfalls could be categorised into three phenomenological types. Type A (n = 19, i.e., 38.8 %) shows a single short pulse of seismic energy. The pulse lasts less than 2 s and predominantly exhibits frequencies between 5 and 50 Hz. Type B (n = 19, i.e., 38.8 %) was characterised by two or more distinct pulses of seismic energy. The frequency range and duration of individual pulses was similar to type A. Type C (n = 11, i.e., 22.4 %) shows an emergent onset and a longer tail of seismic activity, usually lasting 3 to 6 s, sometimes up to 20 s. The frequencies are also in the range of 5 to 40, and sometimes up to 50 Hz. Events of type A and B (n = 21) can show the subsequent emergence of a type C sequence $2.50^{+2.90}_{-0.90}$ s after the last impact signal. This subsequent phase was best visible at seismic stations along the base of the cliff. Twelve events also showed a subdued signal prior to the first significant pulse of seismic energy, which was mostly visible in waveforms of one or two stations along the cliff top. This signal precedes the first major signal pulse by $2.35^{+1.28}_{-1.00}$ s and lasts for less than a second. Three rockfall events have been selected for a detailed description because they allow significant insight into the evolution of the processes and illustrate the summary of results given above.

4.2.1 Case event I

Records from April 6 2015, 15:19:00 to 15:25:00 show two distinct seismic events (figure 2). Both events are recorded at all four functioning stations. The first one shows the arrival of two pulses with sharp onsets and a more than one minute long coda. All stations record this pattern in almost the same shape and intensity; amplitudes at station ”Funny Rain“ are twice as high as at the other stations. The second event is clearly different: the seismogram from “Funny Rain“ shows a sharp amplitude excursion for less than 2 s, followed by an emergent onset of activity for 30 s. The other seismograms only show the first pulse. When filtered between 1 and 3 Hz (figure 2 a insets), it becomes clear that the 1.5 second long signal exhibits arrival time offsets between 70 and 450 ms among the stations. Power spectral density estimates of the vertical component of the ”Funny Rain“ record (figure 2 b) show that the first event is dominated by frequencies between < 1 and up to 60 Hz, with lower frequencies arriving earlier and lasting longer than higher frequencies (triangular pattern). The second event shows a sharp pulse over the entire frequency range above 5 Hz that drops rapidly to a triangular shape of frequencies below 40 Hz. This second signal was a combination of type A and C, with no pause between the two types.

4.2.2 Case event II

Case event II (figure 3) is a complex sequence of 5 discrete pulses, which can be interpreted as a type B event (pulses 1–3), followed by a type C (pulse 4) and a type A event (pulse 5). All pulses last for less than 2 s except for pulse 4, which emerges 6–7 s after pulse 3 and lasts more than 30 s until it is no longer discernible from the background noise. Pulse 5 is intersecting with pulse 4. Signal amplitudes for pulses 1, 2, 3 and 5 are high compared to pulse 4 at station ”Basejumper’s Mess“ whereas this pattern is exactly reversed at station “Funny Rain“, where pulse 4 dominates. Likewise, with increasing distance to ”Basejumpers Mess“, all signals decline in amplitude and become more conjoined for the stations on top of the cliff. Only at “Basejumper’s Mess“ (± 0.6 μm s^{-1}) and very faintly at ”Gate of China“ (± 0.03 μm s^{-1}), there is a signal visible that precedes the entire sequence (pulse 0). The same short duration pulses are also visible in the power spectral density estimates (figure 3 b). Pulse 0 ranges between 50 and 80 Hz at station “Basejumper’s Mess“; all other pulses cover the full frequency range. In contrast, station “Funny Rain“ predominantly exhibits lower frequencies, up to 60 Hz for the short duration pulses and up to 40 Hz for the longer pulse 4, which shows an evolution similar to that of the event described in case 1 (figure 2).

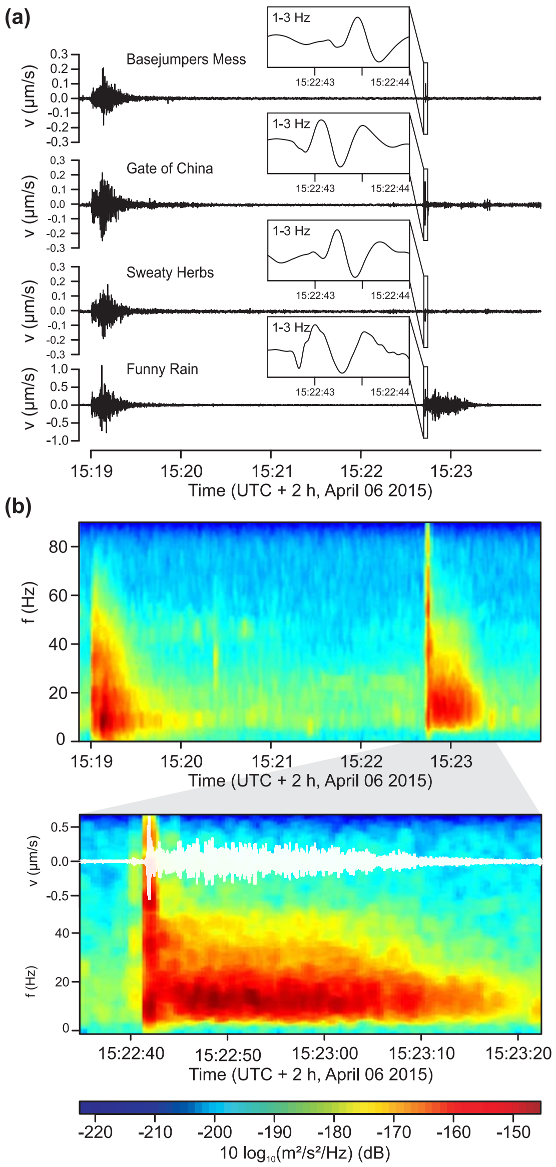

Figure 2. Seismic data of two detected seismic events. a: Waveform data (0.5–90 Hz) starting with a small earthquake on April 6 2014 15:19 that shows the typical P- and S-wave arrivals and coda. 3.6 minutes later, a rockfall was detected, showing a very different, distinct waveform pattern. Inset shows lowpass-filtered (1-3 Hz) signals of the initial rockmass impact with clear time offset between the seismic stations. b: Power spectral density estimates of the earthquake and rockfall as recorded by the vertical component of station “Funny Rain“. The zoomed part shows the waveform of the rockfall again.

Location estimates of the seismic sources were possible for all pulses when adjusting the location approach frequency windows to the dominant frequency content of the signals (figure 3 c and d). While estimates for pulses 1–3 overlap, there is a clear

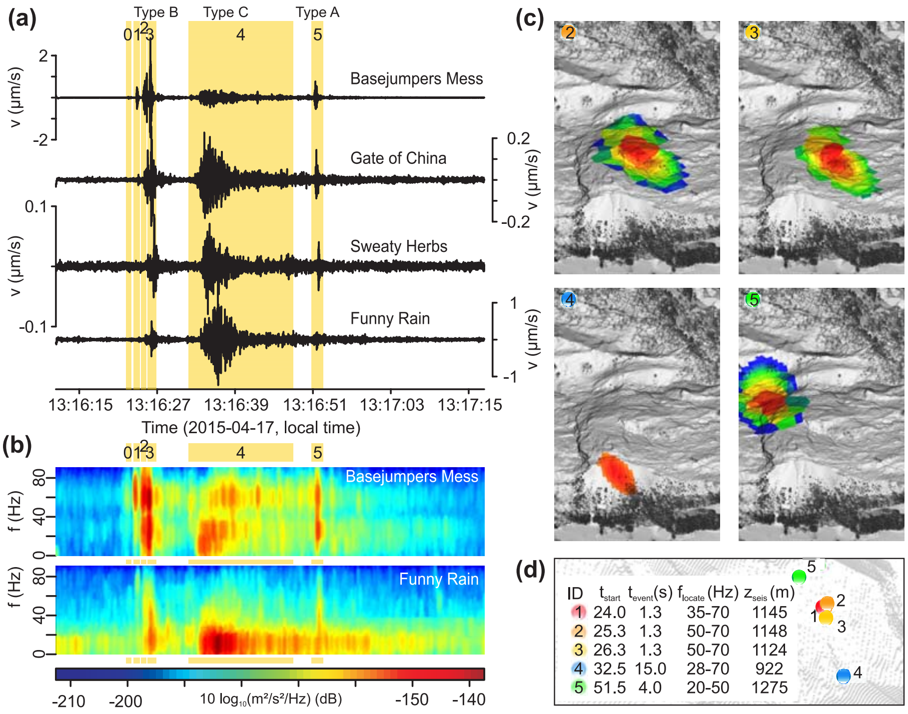

Figure 3. Seismic view of a complex rockfall event. a: signal waveforms of the sequence from four seismic stations, filtered between 0.5 and 90 Hz with four distinct seismic pulses and a longer emergent part. b: Power spectral density estimates of station "Basejumper's Mess" and "Funny Rain". The five distinct events cover different frequency ranges over both, time and space. c: Seismic impact location estimates of event 2 to 5 with maximum probability locations marked by spheres. Scenes show an oblique aerial view onto the lidar-based surface model of the affected cliff section. d: Perspective view on only the maximum probability locations and descriptive measures. t_{start} starting time, t_{event} event duration as used for location, f_{locate} frequency range used for location (based on ranges of all stations), z_{seis} height of location estimate. All times refer to station "Basejumper's Mess".

distinction to pulses 4 and 5. Pulses 1–3 are located at the central cliff part below the large ledge (1148–1124 m asl.), pulse 4 focuses at the base (922 m asl.) and pulse 5 just below the rim of the ledge (1275 m asl.).

4.2.3 Case event III

A rockfall of type B with subsequent emergence of type C (figure 4) occurred on October 26 2014, 22:08:41 local time and lasted about 45 s. Three phases can be distinguished. The first phase was 7.4 s long and characterised by two clear seismic pulses each lasting less than a second and preceded by a subdued signal. The second pulse appears 3.52 s after the first one. The pulses are visible at all stations, although the largest amplitudes occur at station "Funny Rain". Predominant frequencies are between 5 and 50 Hz. Phase 2 starts with a sudden onset of seismic activity 3.38 s after the second strong signal of the preceding phase and lasts 5.8 s. It was also visible at all stations but amplitudes at "Funny Rain" are 500 times higher than,

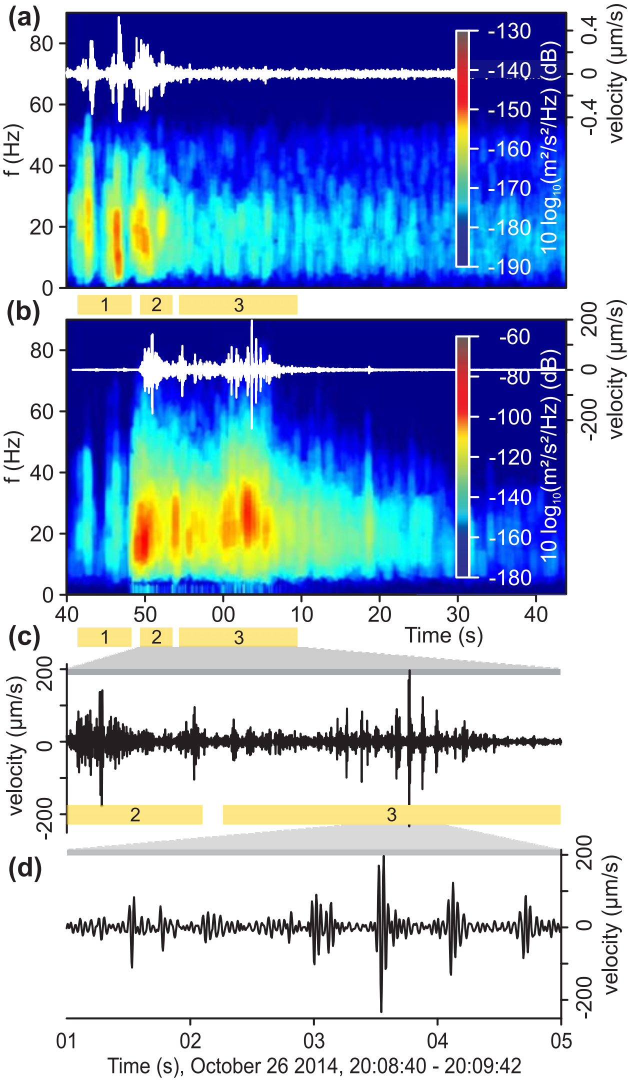

Figure 4. Seismic view of a rockfall (i.e., event 17) with multiple impacts and subsequent rock avalanche. Power spectral density estimate and waveform of stations ”Basejumber's Mess“ (a) and ”Funny Rain“ (b). The station on top of the cliff (a) mainly records the successive impacts along the cliff face, while the basal station (b) reflects the impact on the talus slope and subsequent slope activity. Note the different range of the colour schemes and waveform ranges in (a) and (b). (c) and (d) show zooms into phase 3 as recorded by station ”Funny Rain“. (c) shows the rock mass impact on the talus slope (phase 2) and subsequent activation of a single rock, first rolling then jumping down the slope (phase 3). (d) shows the individual hops of the rock as it approaches and passes the seismic station.

for example at ”Basejumper's Mess“. Phase 3 shows the almost rhythmic appearance of more than 16 pulses in the waveform of station ”Funny Rain“ and was not visible at any other seismic station. The pulses are 0.15 to 0.25 s long and separated by

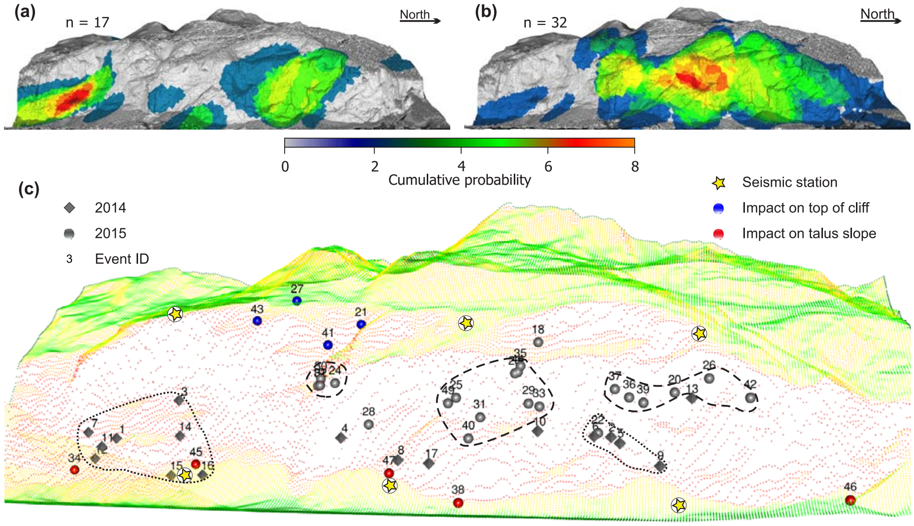

Figure 5. Spatial rockfall activity patterns. a: 3D scene view of compound seismic location estimates for summer/autumn 2014. b: 3D scene view of compound seismic location estimates for spring 2015. Probabilities based on summation of location probabilities > 97 % for all detected events. c: 3D point cloud view of DEM pixels coloured by normalised slope inclination (note the sparse coverage of the steep cliff parts) and maximum location probability of rockfall events as numbered spheres. Blue spheres indicate events at or directly below the cliff edge, red spheres denote events with impact locations at or just above the talus slopes and black spheres denote events in the central cliff part. Cubes depict 2014 events, spheres denote 2015 events. Dotted lines encircle 2014 activity hotspots, dashed lines show 2015 hotspots.

pauses of 0.5 to 0.8 s. The amplitudes of the individual pulses rise slowly until they peak at 20:09:03.5 and then fall back into seismic background levels after about 5 s.

4.3 Spatial activity patterns

The 17 rockfalls recorded in 2014 mostly detached and impacted in the lower southern part of the instrumented cliff section (figure 5 a and c). A minor centre of activity was in the northern part of the cliff. In contrast, most of the 32 rockfalls detected in 2015 detached and impacted at the upper and central parts of the cliff, in the central and northern section (figure 5 b and c). There appear to be three activity hotspots in 2015. The southern one was located just north of the hanging valley of the Ägertenbach (figure 1) and comprises four events. The other two are below the edges of the large ledge in the central part of the steepest and longest cliff section between stations “Gate of China“ and “Basejumper’s Mess“. There, the southern one comprises ten, the northern one six recorded events. Other parts of the instrumented area were affected by single rockfall events (dark blue coloured patches in figure 5 a and b). Five impacts occurred at the base and four near the top of the cliff (figure 5 c).

Earth Surf. Dynam. Discuss., doi:10.5194/esurf-2017-20, 2017
Manuscript under review for journal Earth Surf. Dynam.
Discussion started: 12 April 2017

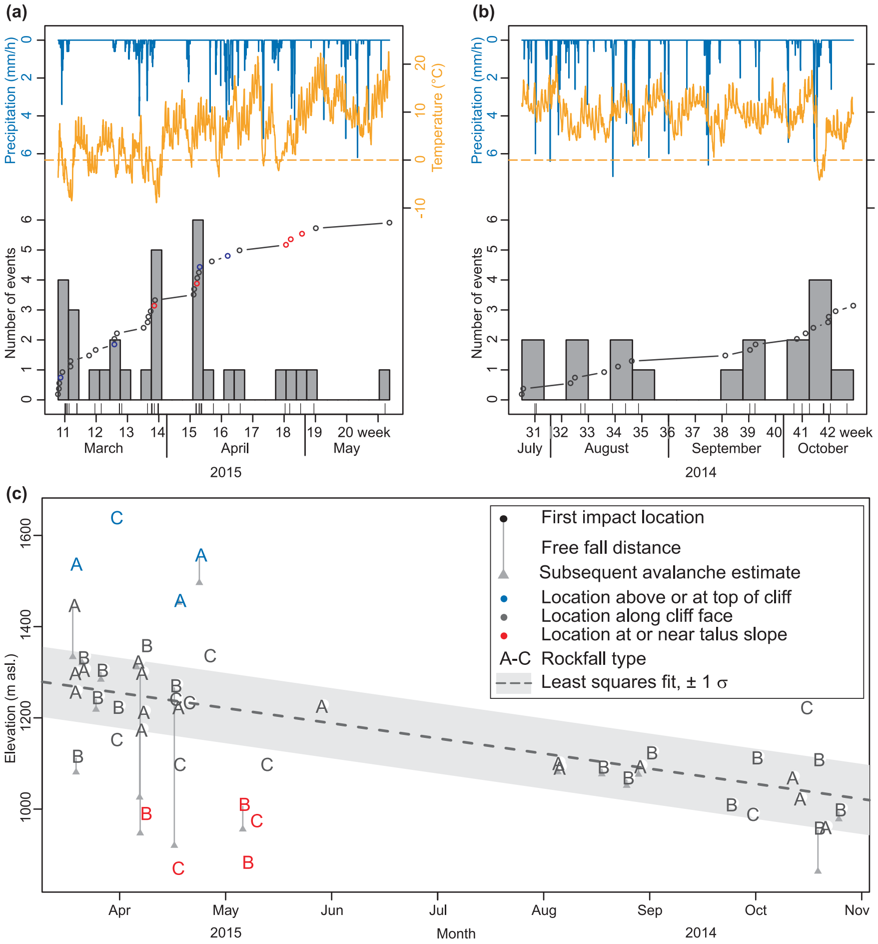

Figure 6. Temporal patterns of rockfall activity. a: times series of all detected rockfalls from spring 2015. b: time series of summer/autumn 2014. Histogram bars and rug show rockfall events, circle-line graph shows cumulative number of events. For the colour of circles, see legend to c. Dashed orange line depicts zero degree. c: Height of the seismically estimated first rock mass impact as function of month of the year (note that 2014 events are plotted right of the 2015 events). Grey vertical lines and triangles give projected downslope displacement (where possible) due to gravitational acceleration and time offset to subsequent avalanche emergences. Letter denotes phenomenological rockfall type.

4.4 Temporal activity patterns

Rockfall activity was distributed over almost the entire instrumented period in both years (figure 6 a and b). However, the distribution was not uniform. In 2014, ten of 14 detected rockfalls occurred in a four-week window during 12 weeks of recording, and three weeks from 2 to 25 August had no activity. Mostly, activity occurred in clusters of two to three events. These patterns of rockfall timing were similar in 2015 although activity was greater and concentrated in the first five weeks of the monitoring window. There were three periods of enhanced activity that account for two thirds of all events: 19–21 March (7 events), 6–9 April (6 events) and 17–21 April (7 events). The rockfalls in these three periods were not clustered in space. There were always more than three cliff sections affected per period and location estimates were never horizontally closer than 40 m to each other, i.e., events close in time were separated by several hundred metres.

When normalised by cliff area (2.16 km^2) the average event rate over the entire instrumented period in 2014 was 2.64 rockfalls per month and km^2. On a month by month basis, we obtain values of 2.78 (August), 0.93 (September) and 4.17 (October). In 2015 the average rate was 5.01 rockfalls per month and km^2. For the four individual months rates were 11.50 (March, only 15 days included), 6.96 (April), 2.32 (May) and 4.11 (June, only 7 days included) per month and km^2.

4.5 Lag time analysis

For all relevant trigger mechanisms the lag times of the 49 detected rockfalls were individually analysed using kernel density estimates. The density estimates of earthquake lag times, i.e., the time passed between an earthquake and the next occurring rockfall, (figure 7 a) peak between 1 and 2 hours, which is almost equal to the lag time between two earthquakes. One rockfall occurred 2 minutes after an earthquake, a second one 3.7 minutes later (i.e., the event from figure 2) and all others at least 12.5 minutes after an earthquake. All these earthquakes were very small local events. The strongest earthquake-related peak ground acceleration value measured by the seismic array was 0.05 ms^{-2} (i.e., 5.1 10^{-3} g) and was more than 8 hours before the next rockfall event. The strongest earthquake from the data base of the Swiss seismological survey within the queried radius of 20 km from the centre point of the cliff was near Brienz (March 29 23:43:22) with Mw = 0.9, occurring about 65 hours before the next rockfall.

The lag time density estimates for precipitation events above 0.1 mm h^{-1} peak at 1 hour. Out of the 49 events, 11 (i.e., 22.4 %) occurred within one hour, and 22 (i.e., 44.9 %) within one day after a rainfall event. There was no difference between the 2014 and the 2015 data and also no systematic trend between lag time and cumulative rainfall amount (R^2 = 0.09, cf. circle size in figure 7 b).

Wind speed during rockfall events ranged from 0 (17 events) to 20.4 (2 events) ms^{-1}. The distribution function of wind speed during rockfalls does not differ from the 1001 distribution functions of each 49 randomly selected hours throughout the data set (figure 7 c).

Lag times for freeze-thaw related rockfalls (figure 7 d) peaked between two and three hours. Thaw-freeze-related events showed lag times of around 12 hours, i.e., they occurred about half a diurnal cycle before a rockfall occurs. Likewise, there were constant, strong linear temperature trends 3, 6 and 12 hours before a rockfall event (figure 7 e). The slope coefficients of the trend lines were closer to one for the rising temperature trends than for the cooling trends. Hence, temperatures rose or fell nearly linearly for 12 hours before a rockfall occurred.

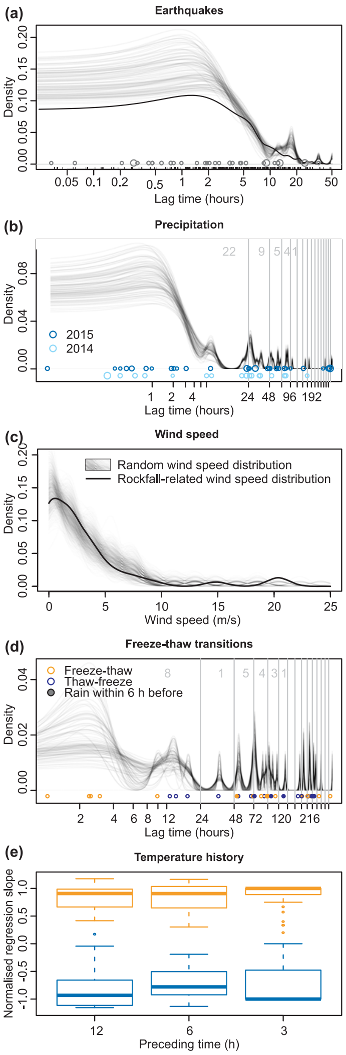

Figure 7. Time lags of all detected rockfall events to different potential triggers as shown by kernel density estimates based on subsampling the rockfall data set and using different kernel sizes. a: Earthquakes. Lag times are of the order of lag times between earthquakes (thick black line). Circle size is proportional to seismic energy of the earthquake signal envelopes. b: Precipitation. Circle size proportional to cumulative rain amount of a preceding event. Circle colour depicts year. c: Wind speed. Thick black line depicts wind speed distribution during rockfall events, grey lines show distributions of randomly selected wind speed samples. d: Freeze-thaw events. Circle colour indicates freeze-thaw (orange) versus thaw-freeze (blue) transitions. Filled circles indicate combination with rainfall within six hours. e: Temperature history before an event, illustrated as slope coefficients of linear regression lines of air temperatures 3, 6 and 12 hours before a rockfall event. Positive (orange) and negative (blue) slopes are separated by colour.

5 Discussion

5.1 Rockfall characteristics

There are three distinct types of rockfall signals. Type A is interpreted as rocks that are released and experience a free fall phase before collision. Except for event 16 (cf. table S1 or figure 5), events of this type did not hit the base of the cliff or the talus slopes directly (figure 6 c). Indeed, half of the type A events exhibit the emergence of a prolonged signal some time after the initial impact, which may be best explained by rock fragments that subsequently reach the cliff base. The event in figure 2 is an example of rockfall type A with a very short pause between first impact and subsequent emergence of the rock fragment avalanche. Rockfalls of type B are interpreted as events that result from multiple impacts, either of the same initial rock volume at subsequently lower parts of the cliff (i.e., example from figure 3) or of different rock masses subsequently detaching from the same source region. For most of the cases it was not possible to distinguish between these two possibilities. Events of type C are interpreted as avalanches of rocks (e.g., prolonged activity in figure 2 b, individual pulse 4 from figure 3, phase 3 from figure 4). Events that are entirely of this type are generally lacking a distinct initial impact of a free falling rock mass. They occur at the base (event 38 and 47), on top of the cliff (event 41), just above the large ledge (26) or near other, less steep or step-structured parts of the cliff (event 39). Rockfall types A and B are equally likely to occur. No type shows any relationship with seismically detected elevation along the cliff (figure 6 c). In summary, the events from the Lauterbrunnen Valley exhibit a considerable range of rockfall scenarios, depending not only on the detachment height but also on the geometry of the cliff, i.e., whether surface topography supports free fall of rocks or causes avalanche-like translocation.

Time differences between first impact and emergence of prolonged avalanche-like activity can be interpreted as free fall time. Converting time to vertical displacement due to gravitational acceleration yields fall distances between about 1 and 286 m, excluding obvious outliers (events 8, 32, 34, 35 and 37 with lag times between 8.4 and 21.0 s) that probably represent remobilisation of material on talus slopes after some lag time. Whether the time difference between the first impact and a preceding seismic signal was related to the detachment process (Vilajosana et al., 2008) or was a result of the first, low energy impact of an already detached rock mass cannot be resolved here.

Location of the seismic signals of rockfalls yields the spot of the first impact, rather than the actual detachment area. Thus, when converting the observed detachment signal time delays to fall distance we need to add 30^{+34}_{-21} m to each event to get an estimate of the real detachment height. This value is well within the location uncertainty range. Thus, we do not correct the location estimate for this effect.

5.1.1 Case event I

The first case event (figure 2) illustrates the fundamental differences between earthquakes and rockfalls from a seismic perspective. At the first glance, both events look similar at station “Funny Rain“. But when including the other seismic stations into the interpretations, the rockfall event was very distinct from the earthquake. It was independent of the preceding earthquake, given the long time gap and low intensity of ground movement. The first evidence of the rockfall was a faint signal 1.5 s before the most powerful signal part, which is hard to see in the waveform but clear in the power spectral density estimate (figure 2 b).

Whether this faint signal represents the detachment of the rockmass or the release of some smaller rocks prior to the large detachment cannot be resolved. The strongest signal, visible at all stations, is interpreted as the actual impact of the rock mass on the cliff face, which leads directly to avalanche-like slope activity for more than 30 s. This last part of the sequence did not give any clear location estimate. The first impact could be located at the northern shoulder of a hanging valley (event 12 in figure 5 c). Apparently, downslope topography was not steep enough to support an immediate free fall phase. A likely scenario is that upon the first impact the rock mass became fragmented and tumbled down the valley shoulder where it might have become further fragmented, then experienced a free fall phase and started hitting the talus slope as a rain of small rock fragments, lasting for more than 30 s. Thus, the seismic data of this rockfall provide insight to all relevant stages: initiation/detachment, free fall, impact and fragmentation, and continuous slope activity caused by impacting and entrained debris.

5.1.2 Case event II

The second case event (figure 3) illustrates how seismic methods can shed light on the complexity and interaction of processes. The described rockfall is of type B (multiple impacts). Like the first example it exhibits a faint seismic signal (pulse 0 in figure 3), about 1 second prior to the first strong impact of rocks recorded by all stations. By combining the information from signal waveforms and power spectral density estimates, a detailed evolutionary scenario can be developed:

- 11:16:24.0 – a weak signal, dominated by high frequency content, was caused by the impact below the large ledge in the central part of the monitored cliff area, at about 1145 m asl.
- 11:16:25.4 – a sharp distinct pulse of seismic energy with highest amplitudes close to station ”Basejumper's Mess“ was caused by an impact of the failed rock mass at an elevation close to the former location (about 1148 m asl.).
- 11:16:26.3 – another pulse of seismic energy was emitted by the already partly fragmented rockmass hitting the cliff face a further time, just about 20 m below the former spot. Upon this impact, the rockmass was further fragmented and falls freely down the rest of the cliff (calm period of about 6.7 s after the impact signals).
- 11:16:32.6 – a sequence of seismic activity, most intense at the base of the cliff close to station ”Funny Rain“, was emerging and lasting for 30 s. In contrast to the preceding impacts, there were no erratic pulses of energy but a continuous, asymmetric rise and fall of the entire signal envelope. This was most likely due to first fragments of the initial rockmass reaching the talus slope below the detachment area and a subsequent continuous rain of particles, the products of the previous fragmentation of the rockmass, for half a minute.
- 11:16:51.8 – Another short pulse of seismic energy, now above the initial impact zone of the first rockfall, was intersecting with the still ongoing shower of rock fragments. This second sharp signal corresponds to the impact of another rockmass about 125 m above the first one, directly at the rim of the large ledge, some 70 m south of the first detachment area. Presumably, this second rockfall was triggered by the impacts of the preceding one.

The location estimates of all events are vague when focusing on the seismic estimates (figure 3 c). In fact, the steep part of the cliff is poorly resolved in vertical direction by only a few DEM pixels (cf. large spacing of dots figure 5 c), which leads to considerable shifts in the maximum location probabilities. Hence, this case shows the lower limit of location possibilities for such extreme topography. However, when calculating the free fall distances based on the time offsets between the individual impact times the agreement is remarkable. Based on the seismic location estimate, the second rock mass impact was located 24 m below the first one, and 4.9 m when applying gravitational acceleration for 1.0 s. Seismic estimates determine the impact at the base, 202 m below the former impact, while gravitational acceleration calculation yields a downslope distance of 200 m after 6.7 s free fall time.

5.1.3 Case event III

The third case (figure 4) illustrates the potential of environmental seismology to resolve multiple failures from the same location and underlines the high degree of detail needed to describe these individual process kinetics of single rocks moving through the landscape. The described rockfall, event 8 of the data set of Dietze et al. (2017), is a combination of type B (during phase 1 and 2) and a special case of type C (during phase 3). Phase 1 is interpreted as two successive impacts along the cliff face. Phase 2 represents the final impact of the rockmass on the talus slope, mobilising a series of rock fragments. Finally, one larger rock fragment starts rolling and jumping down the talus slope, towards and past the station "Funny Rain". The described event is released 0.258 ± 0.014 m^3 from a spot about 994 m asl. The detachment area was just above the seismic station at 888 m asl. and some 20 to 30 m to the North. This implies an independently calculated free fall distance of 106 m. The seismic estimate of the impact was 919 m asl., with the most likely impact coordinates only 52 m away from the seismic station. Converting the time between the first and second impacts of phase 1 (3.52 s) into fall distance yields 122 m. The time offset between the second impact and the onset of phase 2 (3.38 s) represents a similar fall distance of 112 m. A total fall time of 6.9 s would correspond to a fall distance of 795 m, which is not permitted by the cliff height at this section. Thus, in this case, it was possible to show that the two impacts resulted from two discrete detachment events at the same location rather than two discrete impacts of the same released mass at different cliff sections. The data also gives insight into the mechanism by which impacting rock fragments continue to move downslope (short seismic pulses in figure 4 d).

The three examples show the diversity of how rockfalls may evolve and how environmental seismology can provide insights into this geomorphic process that no other method could achieve. A posterior mapping approach would have misinterpreted the two linked events from case 2 (figure 3) as two discrete rockfalls and would have merged the two subsequent rock mass releases from case 3 (figure 4) into a single event.

5.2 Spatial and temporal activity patterns

Rockfall impact areas from seismic monitoring are scattered across the entire area of observation but show distinct horizontal (southern part in 2014 versus three central clusters in 2015) and vertical (basal parts in 2014 versus central and upper parts in 2015) patterns. This short-term variability highlights the necessity to resolve sub-annual time-scales of activity, even below seasonal survey recurrence intervals. 59 % of all events occur in 12 % of the instrumented time in 2015, during three discrete activity periods. Within each of the activity periods the impacts are predominantly laterally spread by more than a kilometre.

Except for one event that stretches into the upper part of the Ägertenbach waterfall, localities of the 2015 data are outside of the hanging valleys where collapsing frozen waterfalls may act as source of seismic signals that might be misinterpreted as rockfalls. The seismic array also detected rockfall events outside the monitored cliff face. These were mainly from two other active areas: the west-facing valley side and the steep east-facing slope of the Chänelegg above the town of Mürren (figure 1 a).

When comparing the seismic-based spatial activity patterns from this survey with the laser scan-based patterns of Strunden et al. (2014) some similarities can be found despite the rather long integration times of the laser scan campaigns. During June–December 2012, 16 rockfalls were released, mainly at the lower cliff part. In contrast, during January–March 2013 the 19 detected rockfalls came from the central and upper part of the cliff. Interestingly, there were no events in the areas of the three activity hotspots of the 2015 seismic monitoring period.

Exploiting the seismic data with much better temporal resolution combined with the location estimates, the above illustrated pattern becomes a clear trend. Over two consecutive years there is a linear trend of, on average, 33.0 m downward shift of rockfall detachment per month, which stretches from 1270 ± 77 m asl. to 1020 ± 77 m asl., which effectively is the cliff base. For 2015 only, the shift amounts to 46.7 m per month and for 2014 it is 36.0 m per month. This suggests a systematic seasonal downward shift of rockfall activity. It remains unclear when (which time of the year) and where (upper limit of activity) this cycle starts without a considerably longer instrumentation period. To shed light onto potential forcing mechanisms of this pattern, we need to first identify the role of trigger mechanisms.

5.3 Trigger mechanisms

Several time scales need to be considered when addressing the relationship between rockfall activity and potential triggers. There may be longer scales (e.g., cyclic adaptations of climate at the order of years to millennia) but the largest one visible in this study – though only barely resolved – is the seasonal scale. The seasonal scale sets the constraints on the effectiveness of individual triggers. For example, freeze-thaw transitions may be expected during winter and spring rather than during summer. Superimposed there is a scale at the order of several days to a few weeks, which mainly reflects the actual weather conditions. Further, there is a diurnal scale that modulates the effect of the prior one, mainly through the effects of sunlight exposure. Finally, there is another small-scale modification of activity patterns, related to the response time of the rock mass to the trigger conditions. This scale is of the order of a few seconds to several hours (cf. 2). Apart from these nested temporal scales in which rockfall triggers manifest, there are also triggers that are completely independent, such as earthquakes, propagation of cracks and anthropogenic activity.

5.3.1 The seasonal scale

The seasonal scale is resolved in this study only with two distinct time periods, late summer to autumn (grading from the highest towards moderate temperatures and from the moistest to the driest conditions) and late winter to spring (grading from the lowest to moderate temperatures and from frozen to liquid water dynamics). The last four rockfalls in 2014 occurred after a temperature excursion below 0 °C. The first two periods of enhanced rockfall activity in 2015 were associated with freeze-thaw cycles and rainfall. Accordingly, freeze-thaw-related rockfalls occur only in the late autumn and early spring period. However, four out of the five rockfalls with a freeze-thaw-transition time lag below about half a day have precipitation lag times of less than one hour, which makes it difficult to argue for temperature as the predominant trigger at this seasonal scale.

5.3.2 The weather-relevant scale

The meteorologically dominated scale is expressed by the three activity periods in 2015 that coincide with strong shifts in temperature, sometimes below zero degrees, but mostly with precipitation events (fig. 6). Accordingly, the precipitation-related lag times, peaking around 1–2 h (fig. 7 b), suggest a strong link between rain and rockfall occurrence. Other studies (Hibert et al., 2014; D'Amato et al., 2016) found similar strong links between rockfall activity and precipitation. However, the small lag time implies that a temporal resolution of several hours (D'Amato et al., 2016) is still insufficient to constrain precipitation as trigger. Perhaps even the hourly aggregated meteorological data used in this study is not detailed enough.

The meteorological time series contains 108 rainfall events with at least 0.1 mm/h cumulative precipitation (0.2 was the minimum cumulative amount recorded preceding a rockfall in this study). However, this does not mean that every second rainfall event caused a rockfall. In September 2014 and June/July 2015 there were multiple rainfall events without any rockfall. Vice versa, the two prominent rockfall episodes in late May and late April were not associated with any rainfall or with an exceptionally strong rainfall event (cf. figure 6).

5.3.3 Diurnal scale

Nested into this meteorological framework, bulk rockfall activity shows a bimodal diurnal pattern, peaking at 8 am and 8 pm (figure 8 a, grey lines). However, when grouping the events based on their lag times to meteorological phenomena, this bulk pattern changes considerably (fig. 8 d). The 16 strongly precipitation-related rockfalls (i.e., events with lag times smaller than 4 h, coinciding with the significant drop of the KDE, cf. fig. 7) form a bimodal distribution with modes at 3–8 am and 6–10 pm, which evidently reflects the overall rainfall pattern at diurnal scales regardless of the season. Subtracting these precipitation-related and the freeze-thaw-related events from the global data set yields only those events that are not related to weather phenomena, keeping in mind that wind speed during rockfalls is not different from random wind speed and that there were no signals of lightning strikes visible in the seismic data. These 26 weather-insensitive rockfalls can be roughly assigned to four groups (grey polygons in fig. 8 d) that do in turn correspond to the diurnal temperature cycle (fig. 8 b). Namely, the group from 0–6 am corresponds to the coldest hours of the day, just before daylight, when thermal contraction of the rock is highest and causes the highest stresses. The group from 8–11 am lags the strongest positive temperature change rates by 1–3 h. This correspondence reflects the strongest stress increase due to thermal input, including a 2–3 h heat diffusion time lag (cf. Collins and Stock, 2016). In analogy, the group from 3–5 pm represents the opposite to the former case, with negative temperature change rate. The last group from 7–11 pm appears to be independent from thermal forcing.

Hence, from this detailed insight into the relations of individual events to potential meteorological and solar drivers there appear to be three relevant and independent causes of rockfall in the Lauterbrunnen Valley: i) insolation and heat diffusion that drive thermal expansion and contraction of the rock (17 of 49 rockfalls), ii) precipitation (19 of 49 rockfalls), and iii) freeze-thaw transitions, perhaps combined with precipitation (5 of 49 rockfalls), leaving 8 rockfalls triggered by other mechanisms

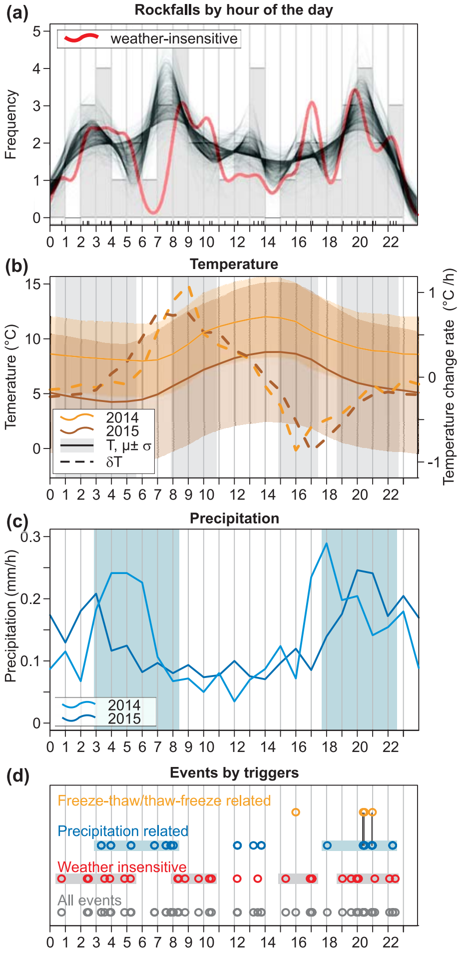

Figure 8. Rockfall activity and potential drivers/triggers grouped by the hour of the day. a: Histogram with 1 h wide bins is overlaid with Monte Carlo-based kernel density estimates (grey lines, kernel size changed between 0.5 and 2 h) and a deterministic KDE (kernel size 0.8 h) of the weather-insensitive events. b: Daily air temperatures (solid lines and polygons) and temperature change rates (dashed lines) for summer/autumn 2014 and spring 2015. c: Average precipitation for the two instrumented periods. d: Individual events grouped by drivers. Freeze-thaw-related is defined as time lags < 4 hours (cf. density drop after that time in fig. 7 d). Precipitation-related is defined as time lags < 8 hours (cf. density drop after that time in fig. 7 b). Weather-insensitive is defined as being neither freeze-thaw- nor precipitation-related.

or with longer lag times to the above triggers. Collins and Stock (2016) observed a strong diurnal pattern in extension and contraction of cracks in exfoliating rock slaps in the Yosemite Valley and argue that insolation may cause some of the rockfalls that could not be attributed to any other trigger mechanism. Here, we can show how and during which preferred time of the day this cyclic forcing actually leads to rockfalls.

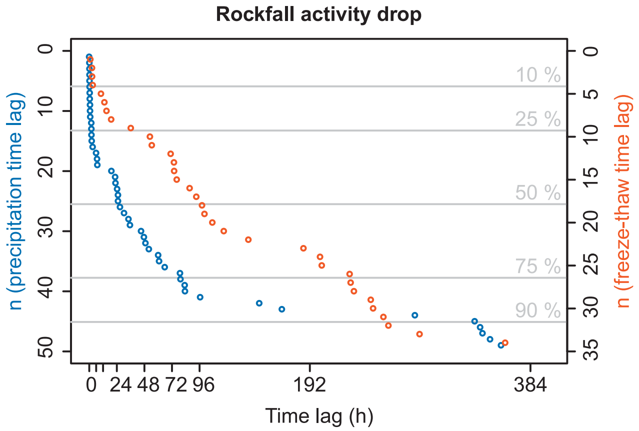

Figure 9. Activity drop with time, grouped by triggers (restricted to data with time lags < 385 h). The data sets are ordered by their lag time to the preceding trigger events. For precipitation, about 50 % of all events occur within one day after a precipitation event, while only 25 % of freeze thaw-related events occur during this period.

The lag time information can also be used to provide estimates of the risk of experiencing a rockfall after a meteorological trigger scenario, such as a rain storm or thawing conditions (fig. 9). Almost 50 % of all rockfalls detach within the first day after a precipitation event, predominantly during the first few hours. Freeze-thaw-related rockfalls show a much weaker pattern with only 25 % occurring within one day after a freeze-thaw transition.

5.3.4 Time scale-independent triggers

Earthquakes appear to be irrelevant for rockfall activity in the Lauterbrunnen Valley. Although the lag time of a rockfall to an earthquake is between one and two hours and can be as short as a few minutes, this relationship is spurious and reflects the recurrence time distribution of earthquakes rather than the link to rockfalls (figure 7 a). The strongest recorded nearby earthquake (Mw 0.9) is hardly able to cause any major ground motion in the study area (though it was recorded by the deployed sensors), as is also reflected by almost three days until a rockfall occurred. Interestingly, 9 of the 49 events showed the seismic signature of a helicopter passing by, 10 to 5 minutes before a rockfall occurred. However, small ground accelerations of $< 10^{-3}$ ms^{-2} make a direct influence unlikely.

5.4 Cause of the vertical rockfall activity trend

In spring, when the freeze-thaw trigger is relevant, only the upper parts of the cliff are active, as these receive sufficient sunlight to drive transitions between ice and liquid water. Indeed, through the course of the month of March the upper rim of the Lauterbrunnen Valley can potentially receive from 8 to 12 hours of sunlight per day, while the cliff base receives only from as little as 3 to about 8-10 hours of sunlight. Most parts of the cliff receive less than 4 hours of sunlight at the beginning of March and can gain between 6 and 12 hours at the end of this month. The lower limit of the sunlit part of the cliff continuously

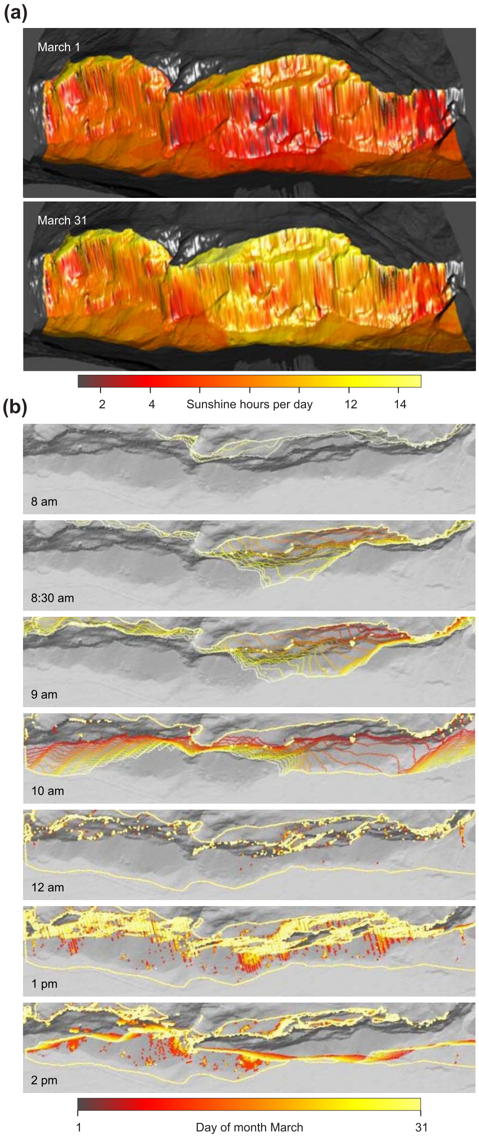

Figure 10. Potential sunshine coverage of the western Lauterbrunnen cliff face. a: Cumulative potential sunshine hours for the beginning and end of March 2015. The central part of the cliff shows the most changes, from 2–6 hours on March 1 to 6–14 hours at the end of this month. b: Sunlight-covered areas along the cliff face for different hours of the day (individual panels) and through the course of March 2015 (colour of the lines). The cliff cannot receive sunlight before 8 am, is completely in the sun by noon and in the shadow again around 1 pm. Again, the central cliff part is the most sensitive during 8 and 10 am. Sunlight polygons clipped to area of interest from figure 1

lowers throughout March, especially considering the early hours of a day (figure 10 b). For example, at 8 am there will never be sun on any part of the cliff regardless of the day of the month, whereas at 8:30 am at the beginning of March only the top part of the cliff is exposed to sunlight and the entire cliff is exposed by the end of the month. Thus, throughout early spring, lower sections of the cliff are consistently longer exposed to sunlight and the corresponding heat input. During later parts of the year, as the sun angle increases further, this disproportional pattern diminishes. Accordingly, the most likely time for resetting the downward activity shift to the upper part of the cliff should be late winter to early spring, as has been proposed for other rockfall-prone alpine environments (e.g., Matsuoka and Sakai, 1999). During that time only the upper parts of the cliff experience numerous freeze-thaw transitions (cf. 6 b) and thereby loose the ice as cohesive crack filling.

For the rest of the year, where we also see the downward trend of rockfall activity with time and differential sunlight exposure can no longer be responsible, another mechanism is required. More specifically, this mechanism must include the sensitivity of the cliff to precipitation events and thermal stress due to heat input and diffusion. We see the most plausible underlying mechanism in a continuously lowering drying front along the cliff face, which is restored during late autumn to early spring when the cliff is continuously less exposed to sunlight, the major agent of external drying of the rock wall. Water storage is also refreshed by snow melting higher up in the catchment, which provides a more or less continuous supply of water that can seep into the karstic limestone plateau on top of the cliff during the melt season. Field observations are consistent with this drying hypothesis, as seepage out of the cliff is widespread in March, but by August/September, the cliff is dry outside of precipitation events (cf. figure S1). The presence of a vertically shifting window rather than a continuously widening band of activity suggests a limited potential of a cliff area to release rockfalls once it is appropriately stimulated by a trigger mechanism. In other words, once a given section of the cliff is devoid of all mobile rock mass it needs considerable time (at least until the next lapse of the annual cycle) to allow block production processes, such as weathering, dissolution or crack propagation, to create new mobile material that can be released by a trigger mechanism. Thus, while the dry front moves downward it continuously exposes new cliff sections to the action of trigger mechanisms that are able to cause rockfalls sufficiently fast to keep track with a downward shift of 33 m per month.

But what is the link between a transition from continuously wet to predominantly dry internal rock state and rockfall susceptibility to precipitation and thermal stress? Precipitation leads to a saturation of the rock mass from the surface inwards, provided the rain event is sufficiently long and intense. However, infiltration and migration of the wetting front into the rock mass only occurs if the medium is not yet saturated, i.e., has a negative matrix potential. Thus, only already internally dry cliff sections can experience cyclic wetting and drying, a pattern we attribute to support destabilisation of rock masses and ultimately rock detachment. Thermal stress is a function of temperature change, which in turn depends on heat input, heat conductivity and heat capacity of the medium. The latter parameter takes a value below 1000 J kg^{-1} K^{-1} for limestone, but more than 4000 J kg^{-1} K^{-1} for liquid water. Thus, as soon as the limestone cliffs contain water, their heat capacity increases, and consequently, their susceptibility to thermal stress drops significantly. This trend gets even stronger when assuming water circulation, which leads to effective conveyance and extensive dissipation of heat. Thus, a dry limestone cliff section experiences significantly higher temperature amplitudes and, accordingly, thermal stress inside the rock mass.

Apparently, there is an overlap of the freeze-thaw driven rockfall activity and precipitation-controlled events, whereby the former system is only relevant in the spring period. This pattern is clearly reflected in the monthly aggregated rockfall rates, which range from 11.50 events per km^2 in March and 6.96 events per km^2 in April to values between 4.17 and 0.96 events per km^2 for the other instrumented months.

6 Conclusions

The ability of a seismic network to provide spatial and temporal information on catchment-wide rockfall patterns as well as profound insight into individual stages of single events renders seismic monitoring a universal tool to investigate an important geomorphic process that is otherwise hard to constrain. Insight to event anatomies sheds light onto the variability of the rockfall process. It is possible to detect rockfall activity even before the first network-wide registered impact signals. The number and consequences (e.g., fragmentation) of individual impacts can in principle be resolved. Time spans between these impacts allow calculation of free fall distances and provide the base for exploring energetic relationships of this mass wasting process. The modes of subsequent slope activity – instantaneous deposition, debris avalanches, single rock jumps – allow assessment of process coupling and connectivity analyses. Combining this detailed information about each event reveals that rockfall in the Lauterbrunnen Valley can cause i) one single impact, ii) two or more discrete contacts of an intact rock mass with the cliff, or iii) a rather avalanche-like movement of multiple rock fragments.

Rockfall detection and location allows insight to the temporal and spatial variability of rockfall events well below sub-annual time scales. Although this study only provides a first glance at the spatial and temporal variability of rockfalls in steep alpine terrain, and much longer deployment periods are needed (e.g., to cover at least two full annual cycles), the patterns emerging from the highly variable nature of events could give essential input to rockfall susceptibility models and help improving early warning or mitigation strategies. During different seasons rockfall affects laterally and vertically distinct sections of the cliff. More specifically, spatially different sunlight exposure patterns are only relevant to understand freeze-thaw-related rockfalls during a small time window in spring, whereas the most likely cause for a continuously downward shifting window of rockfall activity over the year seems to be a lowering water table inside the limestone cliff. This implies a spatial and temporal interplay between block production (i.e., transformation of stable cliff sections to rockfall prone entities by ice segregation, thermally driven crack expansion or limestone dissolution) and water and heat related activation of the prepared sections by episodic and diurnally forced trigger mechanisms.

We quantify the relative effectiveness of rockfall triggers. Freeze-thaw transitions account only for 5 (10 %) rockfalls, though precipitation perhaps also plays a role for these, and this trigger is only important during a few cold months of the year. Precipitation is relevant for 19 (39 %) rockfalls year round and 17 (35 %) rockfalls are triggered by diurnal temperature changes although through different mechanisms: 7 (41 %) of these 17 events occur during the coldest hours of the day due to contraction of the rock mass and the highest tensions along crack boundaries, 6 (35 %) occur when the heating rate is highest, i.e., when thermal expansion stress rate is highest, and 4 (24 %) occur during the highest cooling rates, i.e., the opposite direction of the former process. Beyond these 17 rockfalls another 7 events occured during the first half of the night without any identified cause. When focusing on the precipitation-related lag time, 11 (22 %) of all rockfalls occur within 1 hour after precipitation and 22 (44 %) within 24 hours. In other words, almost half of the rockfalls can be avoided when omitting hiking or other activities in rockfall-prone areas for a day after a precipitation event.

For all lag time studies to investigate trigger roles, the final temporal resolution is given by the lowest resolution of all applied techniques: rockfall detection technique, meteorological data, seismic event catalogue, and information about human activity. So far, hourly resolution is the best that could be achieved, limited by the time resolution of the available meteorological data. One way to go beyond this is substituting the meteorological data by seismic signals of precipitation (Roth et al., 2016) and the temperature data automatically registered at the Cube^3 data loggers. Both parameters can be measured at arbitrary high temporal intervals and, more important, at each seismic station. This allows for much better spatial resolution of the meteorological boundary conditions.

7 Data and code availability

The supplementary material contains the raw seismic traces from the recording seismic stations of all rockfalls with a time buffer of 30 s before and after the detected events. The raw point cloud data from the TLS survey is available upon request.

Author contributions. Michael Dietze contributed to seismic fieldwork and data analysis. Kristen L. Cook contributed to terrestrial laser scanning and seismic station maintenance. Jens M. Turowski and Niels Hovius contributed to equipment provision, field work planning and data analysis. All authors contributed to manuscript preparation.

Acknowledgements. The field work campaigns generously benefited from the support of Maggi Fuchs, Michael Krautblatter, Torsten Queißer and Fritz Haubold. The authors are thankful for these creative involvements. We are also thankful to the GIPP seismic device pool for providing six TC120s sensors and Cube^3 data loggers. Solmaz Mohadjer and Todd Ehlers are thanked for joined field work and data discussions.

References

Adler, D. and Murdoch, D.: rgl: 3D Visualization Using OpenGL, https://CRAN.R-project.org/package=rgl, r package version 0.95.1441, 2016.

Bivand, R. S., Pebesma, E. J., and Gomez-Rubio, V.: Applied spatial data analysis with R, Springer, 2013.

Blaauw, M.: Out of tune: the dangers of aligning proxy archives, Quaternary Science Reviews, 36, 38–49, 2012.

Burtin, A., Hovius, N., Milodowski, D. T., Chen, Y.-G., Wu, Y.-M., Lin, C.-W., Chen, H., Emberson, R., and Leu, P.-L.: Continuous catchment-scale monitoring of geomorphic processes with a 2-D seismological array, Journal of Geophysical Research, 118, 1956–1974, doi:0.1002/jgrf.20137, 2013.

Burtin, A., Hovius, N., McArdell, B. W., Turowski, J. M., and Vergne, J.: Seismic constraints on dynamic links between geomorphic processes and routing of sediment in a steep mountain catchment, Earth Surface Dynamics, 2, 21–33, doi:10.5194/esurf-2-21-2014, 2014.

Burtin, A., Hovius, N., and Turowski, J. M.: Seismic monitoring of torrential and fluvial processes, Earth Surface Dynamics, 4, 285–307, doi:10.5194/esurf-4-285-2016, 2016.

Collins, B. and Stock, G.: Rockfall triggering by cyclic thermal stressing of exfoliation fractures, Nature Geoscience, 9, 395–400, 2016.

Corripio, J. G.: insol: Solar Radiation, https://CRAN.R-project.org/package=insol, r package version 1.1.1, 2014.

D'Amato, J., Hantz, D., Guerin, A., Jaboyedoff, M., Baillet, L., and Mariscal, A.: Influence of meteorological factors on rockfall occurrence in a middle mountain limestone cliff, Natural Hazards and Earth System Sciences, 16, 719–735, doi:10.5194/nhess-16-719-2016, 2016.

Dammeier, F., Moore, J. R., Haslinger, F., and Loew, S.: Characterization of alpine rockslides using statistical analysis of seismic signals, Journal of Geophysical Research, 116, F04 024, doi:10.1029/2011JF002037, 2011.

Dietze, M.: eseis: Environmental seismology toolbox, r package version 0.3.1, 2016.

Dietze, M., Kreutzer, S., Burow, C., Fuchs, M. C., Fischer, M., and Schmidt, C.: The abanico plot: Visualising chronometric data with individual standard errors, Quaternary Geochronology, 31, 12–18, 2016.

Dietze, M., Mohadjer, S., Turowski, J. M., Ehlers, T. A., and Hovius, N.: Validity, precision and limitations of seismic rockfall monitoring, Earth Surface Dynamics Discussions, 2017, 1–23, doi:10.5194/esurf-2017-12, http://www.earth-surf-dynam-discuss.net/esurf-2017-12/, 2017.

Ekström, G. and Stark, C. P.: Simple Scaling of Catastrophic Landslide Dynamics, Science, 339, 1416–1419, doi:10.1126/science.1232887, 2013.

Farin, M., Mangeney, A., Toussaint, R., Rosny, J. d., Shapiro, N., Dewez, T., Hibert, C., Mathon, C., Sedan, O., and Berger, F.: Characterization of rockfalls from seismic signal: Insights from laboratory experiments, Journal of Geophysical Research: Solid Earth, 120, 7102–7137, doi:10.1002/2015JB012331, 2015.

Galbraith, R. F. and Roberts, R. G.: Statistical aspects of equivalent dose and error calculation and display in OSL dating: An overview and some recommendations, Quaternary Geochronology, 11, 1–27, 2012.

Gimbert, F., Tsai, V. C., and Lamb, M. P.: A physical model for seismic noise generation by turbulent flow in rivers, Journal of Geophysical Research, 119, 2209–2238, doi:10.1002/2014JF003201, 2014.

Haberkorn, A., Wever, N., Hoelzle, M., Phillips, M., Kenner, R., Bavay, M., and Lehning, M.: Distributed snow and rock temperature modelling in steep rock walls using Alpine3D, The Cryosphere Discussions, doi:doi:10.5194/tc-2016-73, 2016.

Havskov, J. and Alguacil, G.: Instrumentation in earthquake seismology, Modern Approaches in Geophysics 22, Springer, 2006.

Helmstetter, A. and Garambois, S.: Seismic monitoring of Sechilienne rockslide (French Alps): Analysis of seismic signals and their correlation with rainfalls, Journal of Geophysical Research, 115, F03 016, doi:10.1029/2009JF001532, 2010.

Hibert, C., Mangeney, A., Grandjean, G., and Shapiro, N. M.: Slope instabilities in Dolomieu crater, Réunion Island: From seismic signals to rockfall characteristics, Journal of Geophysical Research, 116, F04 032, doi:10.1029/2011JF002038, 2011.

Hibert, C., Mangeney, A., Grandjean, G., Baillard, C., Rivet, D., Shapiro, N. M., Satriano, C., Maggi, A., Boissier, P., Ferrazzini, V., and Crawford, W.: Automated identification, location, and volume estimation of rockfalls at Piton de la Fournaise volcano, Journal of Geophysical Research, 119, 1082–1105, doi:10.1002/2013JF002970, 2014.

Hijmans, R. J.: raster: Geographic Data Analysis and Modeling, https://CRAN.R-project.org/package=raster, r package version 2.5-8, 2016.

Kappus, M. E. and Vernon, F. L.: Acoustic Signature of Thunder from Seismic Records, Journal of Geophysical Research, 96, 10 989–11 006, 1991.

Knight, J. and Grab, S.: Lightning as a geomorphic agent on mountain summits: Evidence from southern Africa, Geomorphology, 204, 61–70, 2014.

Krautblatter, M., Verleysdonk, S., Flores-Orozco, A., and Kemna, A.: Temperature-calibrated imaging of seasonal changes in permafrost rock walls by quantitative electrical resistivity tomography (Zugspitze, German/Austrian Alps), Journal of Geophysical Research: Earth Surface, 115, n/a–n/a, doi:10.1029/2008JF001209, f02003, 2010.

Krautblatter, M., Moser, M., Schrott, L., Wolf, J., and Morche, D.: Significance of rockfall magnitude and carbonate dissolution for rock slope erosion and geomorphic work on Alpine limestone cliffs (Reintal, German Alps), Geomorphology, 167-168, 21–34, doi:10.1016/j.geomorph.2012.04.007, 2012.

Lacroix, P. and Helmstetter, A.: Location of Seismic Signals Associated with Microearthquakes and Rockfalls on the Séchilienne Landslide, French Alps, Bulletin of the Seismological Society of America, 101, 341–353, doi:10.1785/0120100110, 2011.

Larose, E., Carrière, S., Voisin, C., Bottelin, P., Baillet, L., Guéguen, P., Walter, F., Jongmans, D., Guillier, B., Garambois, S., Gimbert, F., and Massey, C.: Environmental seismology: What can we learn on earth surface processes with ambient noise?, Journal of Applied Geophysics, 116, 62–74, doi:10.1016/j.jappgeo.2015.02.001, 2015.

Martinez, A. R., Roubinet, D., and Tartakovsky, D. M.: Analytical models of heat conduction in fractured rocks, Journal of Geophysical Research: Solid Earth, 119, 83–98, doi:10.1002/2012JB010016, 2014.

Matsuoka, N. and Sakai, H.: Rockfall activity from an alpine cliff during thawing periods, Geomorphology, 28, 309–328, 1999.

Nychka, D., Furrer, R., Paige, J., and Sain, S.: fields: Tools for spatial data, doi:10.5065/D6W957CT, www.image.ucar.edu/fields, r package version 8.4-1, 2015.

Pebesma, E. J. and Bivand, R. S.: Classes and methods for spatial data in R, R News, 5, 2005.

Pebesma, E. J. and Bivand, R. S.: sp: Classes and Methods for Spatial Data, https://CRAN.R-project.org/package=sp, r package version 1.2-3, 2016.

R Development Core Team: R: A Language and Environment for Statistical Computing, Vienna, Austria, http://CRAN.R-project.org, 2015.

Roth, D. L., Brodsky, E., Finnegan, N., Rickenmann, D., Turowski, J., and Badoux, A.: Bed load sediment transport inferred from seismic signals near a river, Journal of Geophysical Research Earth Surface, 121, 725–745, doi:10.1002/2015JF003782, 2016.

Service, S. S.: WebDC3 Web Interface to SED Waveform and Event Archives, Available at http://arclink.ethz.ch/webinterface/ (2014/09/29).

Stock, G., Collins, B., Santaniello, D., Zimmer, V., Wieczorek, G., and Snyder, J.: Historical rock falls in Yosemite National Park, U.S. Geological Survey Data Series 746, 746, 17, 2013.

Stock, G. M., Bawden, G. W., Green, J. K., Hanson, E., Downing, G., Collins, B. D., Bond, S., and Michael Leslar, M.: High-resolution three-dimensional imaging and analysis of rock falls in Yosemite Valley, California, Geosphere, 7, 573–581, 2011.

Stoffel, M., Lievre, I., Monbaron, M., and Perret, S.: Seasonal timing of rockfall activity on a forested slope at Täschgufer (Swiss Alps) – a dendrochronological approach, Zeitschrift für Geomorphologie N.F., 49, 89–106, 2005.

Strunden, J., Ehlers, T. A., Brehm, D., and Nettesheim, M.: Spatial and temporal variations in rockfall determined from TLS measurements in a deglaciated valley, Switzerland, Journal of Geophysical Research, 120, 1–23, doi:10.1002/2014JF003274, 2014.

Suriñach, E., Vilajosana, I., Khazaradze, G., Biescas, B., Furdada, G., and Vilaplana, J. M.: Seismic detection and characterization of landslides and other mass movements, Natural Hazards and Earth System Sciences, 5, 791–798, 2005.

Turowski, J. M., Dietze, M., Schöpa, A., Burtin, A., and Hovius, N.: Vom Flüstern, Raunen und Grollen der Landschaft. Seismische Methoden in der Geomorphologie, System Erde, 6, 56–61, doi:10.2312/GFZ.syserde.06.01.9, 2016.

Vilajosana, I., Surinach, E., Abellan, A., Khazaradze, G., Garcia, D., and Llosa, J.: Rockfall induced seismic signals: case study in Montserrat, Catalonia, Natural Hazards and Earth System Sciences, 8, 805–812, 2008.

Welch, P. D.: The use of fast Fourier transform for the estimation of power spectra: A method based on time averaging over short, modified periodograms, IEEE Transactions on Audio and Electroacoustics, 15, 70–73, 1967.

Wieczorek, G.: Landslide triggering mechanisms, in: Landslides–investigation and mitigation, edited by Turner, A. and Schuster, R., pp. 76–90, Transportation Research Board, National Research Council, National Academy Press, 1996.

Zimmer, V., Collins, B. D., Stock, G. M., and Sitar, N.: Rock fall dynamics and deposition: an integrated analysis of the 2009 Ahwiyah Point rock fall, Yosemite National Park, USA, Earth Surface Processes and Landforms, 37, 680–691, doi:10.1002/esp.3206, 2012.